Numerical simulations of NMR relaxation in chalk using local Robin boundary conditions

M. Ögren[a,b,*], D. Jha[a], S. Dobberschütz[a], D. Müter[a],
M. Carlsson[c], M. Gulliksson[b], S. L. S. Stipp[a], and H. O. Sørensen[a]

[a] *Nano-Science Center, Department of Chemistry, University of Copenhagen, Universitetsparken 5, 2100 København Ø, Denmark.*

[b] *School of Science and Technology, Örebro University, 701 82 Örebro, Sweden.*

[c] *Center for Mathematical Sciences, Lund University, Box 118, 22100 Lund, Sweden.*

[*] *Corresponding author: magnus@ogren.se*

Abstract

The interpretation of nuclear magnetic resonance (NMR) data is of interest in a number of fields. In Ögren [Eur. Phys. J. B (2014) **87**: 255] local boundary conditions for random walk simulations of NMR relaxation in digital domains were presented. Here, we have applied those boundary conditions to large, three-dimensional (3D) porous media samples. We compared the random walk results with known solutions and then applied them to highly structured 3D domains, from images derived using synchrotron radiation CT scanning of North Sea chalk samples. As expected, there were systematic errors caused by digitalization of the pore surfaces so we quantified those errors, and by using linear local boundary conditions, we were able to significantly improve the output. We also present a technique for treating numerical data prior to input into the ESPRIT algorithm for retrieving Laplace components of time series from NMR data (commonly called T-inversion).

Key words: NMR-relaxation, random walk, boundary conditions, CT-scanning, T-inversion

1. Introduction

Simulation of particle diffusion through complex media can be used to model many physio-chemical processes in biology, groundwater transport, filtration and for many applications in industry [1]. One can also use the simulated movement of particles to represent diffusing molecules, heat transport, or as here, nuclear magnetic resonance (NMR) excitations carried by protons. NMR based research is of interest in many fields, for example to depict brain tumors [2], in biofilm purification of contaminated water [3], in manufactured porous fiber materials [4], as well as in petrophysical applications [5–7].

When particles interact with a surface or other particles, reactions, reflections or sorption can happen, which changes or interupts the movement of the particles. To describe such systems, a variety of probabilistic mathematical models are used. In the literature, there are reports of the interplay between theoretical and experimental work made on ideal systems of simple geometry, such as glass triangles [8] (and references therein), where exact solutions can be obtained with geometry specific methods. There are also large scale numerical simulations of (digitized) true porous media that have been made by practitioners in various fields, where predictions have been compared with results from experiments. One example is data from core plugs of porous rocks [9, 10]. From what is reported in the literature, quantitative agreement between simula-

tions and measurements is often obtained only after fitting the two data sets with a free parameter or after optimising the surface relaxation parameter, ρ, with the experimental data [11,12]. The value of the surface relaxation parameter used in models strongly affects the NMR decay rate and subsequently the estimated properties of the medium. In reality surface relaxivity is difficult to measure. Therefore most NMR correlations assume constant ρ, even though it is straightforward in stochastic particle models to allow it to be space dependent. For heterogeneous rocks composed of more than one mineral, ρ is not constant and surface relaxivity is reported to increase with higher fractions of microporosity [7].

Despite of how we model the relaxivity, systematic errors may arise in calculated physical properties, because independently of how accurate we solve the problem for the digital domain, the true domain can be quite different from its digitalization. In applications of NMR on rock samples, relaxation is generally slow in the bulk pore volume, V, and relatively faster at the pore surface. Therefore, the description of the surface geometry is essential for simulations. However, in digital domains the surface area, S, does not converge to the true value when resolution increases, in contrast with the behaviour of pore volume, and the methods for treating the surfaces in numerical simulations are critical. Different approaches have been suggested to meet this difficulty [13,14].

This study extends our previous work [15], that used local boundary conditions (LBC) to locally adapt the probability for surface relaxation, p_S, when a NMR excitation encounters the pore surface in the porous medium. For simple domains we have shown that this method closely reproduces the solutions to the corresponding PDE model for which the surface relaxation is controlled by the surface relaxation parameter ρ via a Robin boundary condition [15]. It is clear that development towards more accurate numerical modeling benefit from predictions on well characterised samples, and the purpose of this article is to first carry out benchmarking simulations and then produce results for natural chalk samples.

By starting from two-dimensional artificial porous media of moderate size, we can directly evaluate LBC against results obtained using the finite element method (FEM). For three dimensions we then benchmark the method against analytic solutions for two simple geometries, the ball and the cube. We also rotate the cube with respect to the coordinate system of the digital domain to investigate how LBC works when the surfaces of the cube is not aligned with the faces of the voxels. Finally, the algorithm is used to calculate the NMR relaxation in two different complex geometries of chalk imaged by X-ray tomography and consisting of approximately $10^3 \times 10^3 \times 10^3 = 10^9$ voxels.

1.1. *NMR relaxation model*

The fundamentals behind nuclear magnetic resonance rely on the quantum mechanical magnetic properties of specific atomic nuclei [16], hence "nuclear" and "magnetic". When such a magnet (being placed in an external magnetic field) absorbs energy, the nucleus is described as being in "resonance". This apply, for example, to a porous media filled with water, where the hydrogen nucleus have an intrinsic magnetic moment that can be excited with a radio frequency electromagnetic pulse. The process when the nuclei return to the non-excited state is called relaxation. NMR relaxation analysis of porous media can be used, for example, to estimate permeability, the pore size distribution, and identify pore fluids and gases.

The so called Bloch-Torrey equations [17,18] phenomenologically describe the relaxation dynamics of excited nuclear magnetic moments in the general case. In the case of isotropic diffusion and in the absence of external magnetic field gradients, we get after the termination of the magnetic excitation the remaining single partial differential equation (PDE) describing a magnetic moment $M(\mathbf{x}, t)$ [5,6,19,20] in a pore domain Ω

$$\frac{\partial M}{\partial t} = D_0 \nabla^2 M - \frac{M}{T_V}. \tag{1}$$

This is formally a time dependent heat equation with a source term that is proportional to the magnetic moment. In (1) D_0 is the diffusion constant and T_V is the characteristic time of relaxation in the volume, often called bulk relaxation. At the boundary $\partial\Omega$, we have a mixed Robin boundary condition (BC)

$$D_0 \mathbf{n} \cdot \nabla M + \rho M = 0, \tag{2}$$

where ρ is the surface relaxation parameter. Finally, we need to define an initial condition for the magnetic moment, which we choose to be constant $M(\mathbf{x}, 0) = M_0$ throughout this article. In e.g. [8,15]

other initial conditions are investigated. Uniform initial magnetisation is common in experiments but nonuniform initial conditions can be designed using inhomogeneous radio frequency pulses [21]. In the above PDE model we have assumed that $T_V = T_{V,2}$ ($T_V = T_{V,1}$) and $\rho = \rho_2$ ($\rho = \rho_1$) are for the transverse (longitudinal) component of nuclear spin magnetisation [7,22], i.e., we consider tranverse spin components in the following. Realistic values for the above physical parameters in the three-dimensional case were taken from the literature [12] (and references therein), $D_0 \simeq 2.1 \cdot 10^{-9}$ m^2/s, $T_V \simeq 3.1$ s and $\rho \simeq 1.0 \cdot 10^{-5}$ m/s. The first two parameters refer to water (brine) and the last to a representative brine-chalk interface [9, 10]. For NMR experiments of materials chemically sensitive to water, such as foods, polymers and aerogels, gases (e.g., C_2F_6 and ^{129}Xe) can alternatively be used [23, 24].

In addition to T_V, there are two other characteristic times in the problem. By dimensional analysis we find the diffusion time,

$$T_{D_0} \sim R_0^2/D_0, \tag{3}$$

and the surface relaxation time,

$$T_\rho \sim R_0/\rho, \tag{4}$$

which suggest two limiting regimes dependent on how the typical pore radius R_0 relate to the other parameters. We have *fast diffusion* when $T_{D_0} \ll T_\rho$, i.e., with the parameters above, approximately for $R_0 \ll 100$ μm, and *slow diffusion* in the opposite limit where $T_{D_0} \gg T_\rho$ and $R_0 \gg 100$ μm. Qualitatively, in the *fast diffusion* regime particles carrying a magnetic moment are diffusing to surfaces faster than they are annihilated, resulting in a flat distribution of $M(\mathbf{x}, t)$ for all times, while with *slow diffusion* the number of particles is less close to surfaces and $M(\mathbf{x}, t)$ develops large variations when $\mathbf{x}$ is in the vicinity of the surface. Therefore, if the typical pore sizes are known in respect to the physical parameter values, one can qualitatively predict the dynamics.

Experimentally one often measures the total magnetisation, obtained by integration of the magnetic moment per unit volume over the pore domain Ω

$$\mathcal{M}(t) = \int_\Omega M(\mathbf{x}, t)\, d\mathbf{x}. \tag{5}$$

In this article we study the time dependence of (5) with various methods and boundary conditions.

The article is briefly outlined as follows. In Sect. 2 we present the method we have used to solve the PDE model for NMR relaxation presented above. We tested the numerical method against known results in Sect. 3 and in Sect. 4 we apply the method to NMR relaxation in natural chalk samples and analyse the data in terms of real exponential components. Finally, we present a discussion and a summary of the results in Sect. 5.

2. Method

As pioneered by Kolmogorov, Feynman, Kac, and many others, one can define stochastic processes for many second order PDEs that in the limit of many random realisations may converge to either stationary or time dependent solutions of the PDE [25–28]. A well known example is Eq. (1). In fact the derivation of a diffusion equation is often motivated by a random walk of quasi-particles given by a chemical concentration, a quantity of heat, or as here a magnetic moment carried by protons in water molecules. The additional last term, $-M/T_V$ in (1), is simply modelled using the probability $p_V = \Delta t/T_V$ for the annihilation of every random walker at each time step Δt. However, as long as T_V is considered to be a time and space independent constant, the effect of volume relaxation (V) can be factorized out from the dynamics of the total magnetisation, such that

$$\begin{aligned} M_{T_V}(\mathbf{x}, t) &= \mathrm{e}^{-t/T_V} M_\infty(\mathbf{x}, t), \\ M_{T_V}(\mathbf{x}, t) &\to M_\infty(\mathbf{x}, t),\ T_V \to \infty \end{aligned} \tag{6}$$

holds for any solution of (1). Therefore, hereafter we do not consider the effect of T_V. In the computer implementation this is done by choosing the volume relaxation time very large ($T_V \to \infty$). Consequently, for the results for the chalk samples presented later in the article (Fig. 6) it is necessary to multiply the total magnetisation with a factor e^{-t/T_V} in order to compare with experimental measurements.

2.1. *Cartesian random walk*

The idea here is to use a linear LBC (LLBC) relation between the parameter ρ and the corresponding parameter p_S in a Cartesian lattice based random walk implementation of the problem for a boundary with arbitrary curvature. There are in fact infinitely many degrees of freedom in formulating a corresponding stochastic process for the PDE (1). For example different distributions of random numbers

can be used, and so called gauges can give varying numerical properties while converging to the same solution [29, 30]. Here we use a Cartesian random walk with isotropic step lengths $\Delta r \equiv \Delta x = \Delta y = \Delta z$ where Δr is the resolution (voxel size) of the digital image (Fig. 5). While the computational effort can be dramatically reduced by the introduction of a distance operator to take larger steps when the walkers are far from boundaries [31] we do not exercise this technique here but focus on illustrating the effect of the implemented local boundary conditions. Moreover, the uniform initial condition $M(\mathbf{x}, 0) = M_0$ means that each voxel in the pore-domain Ω is equally likely to be occupied by a random walker at $t = 0$. For a walker at position (x, y, z) and time $t \geq 0$ we then have for $t = t + \Delta t$ that

$$(x, y, z) = (x, y, z) + \Delta r \boldsymbol{r}_j, \tag{7}$$

where

$$\Delta t = \frac{(\Delta r)^2}{6D_0}. \tag{8}$$

In equation (7) $\boldsymbol{r}_j$, $j = 1, 2, ..., 6$ is one of the six unit vectors $\pm \boldsymbol{e}_j$, $j = 1, 2, 3$ and $p(\boldsymbol{r}_j) = 1/6$, or in other words the probability of taking a step of length 1 or -1 in either of the three Cartesian directions is equal.

The total magnetisation (5) in each time step is equal to the number of active trajectories, i.e., the sum over the remaining walkers. This number is normalized in each timestep with the initial number of walkers. Hence the only information needed is the time when a walker is annihilated, which can be easily implemented for parallel computation. Consider a walker taking a step according to (8) that will cross a boundary. Then it has to be decided if the walker is going to be annihilated or reflected back to the original position. In the PDE model for NMR relaxation it is the value of the surface relaxation parameter ρ in Eq. (2) that determines the effect of surface relaxation. More precisely, the BC, Eq. (2), is Dirichlet if $\rho \to \infty$ and Neumann if $\rho \to 0$. For any other value, $0 < \rho < \infty$, we need to relate the surface relaxation parameter in the PDE model to a probability p_S for annihilation of a walker crossing a boundary surface (S). The linear relation

$$p_S = \frac{\Delta r}{D_0}\rho, \tag{9}$$

and other relations, are commonly discussed [8, 13, 32,33]. A derivation of Eq. (9) can be found in Sect. 3 of [15].

2.2. *Local Robin boundary conditions for digital domains*

We first introduce the three-dimensional digital pore-domain Ω in which the diffusion-relaxation dynamics are considered, via the binary phase function

$$Z(\mathbf{x}) = \begin{cases} 1, & \mathbf{x} \in \Omega \\ 0, & \text{otherwise} \end{cases}, \tag{10}$$

where $\mathbf{x} = (x, y, z)$. Characterizations of the digitized media, such as porosity can then be calculated from (10) as $\phi = \sum_{k=1}^{N^3} Z(\mathbf{x}_k)/N^3$, where $\mathbf{x}_k$ is the coordinate for the center of voxel number k and $N\Delta r$ is the side length of the cubic media, see Table 2 for examples. From Eq. (10) we define the boundary $\partial\Omega$ as the two-dimensional pore-surface with one of the outgoing unit vectors $\pm \boldsymbol{e}_j$, $j = 1, 2, 3$ situated a distance $\Delta r/2$ outside the pore-domain, i.e. for which

$$Z(\mathbf{x}) = 1, \; Z(\mathbf{x} \pm \Delta r \boldsymbol{e}_j) = 0. \tag{11}$$

Therefore, the digital surface of the cubic media can be calculated as the point set that fulfills Eq. (11).

In order to construct the linear local boundary conditions (LLBC) for a point $\mathbf{x}$ fulfilling Eq. (11) we need to distinguish between the $2^8 = 256$ possible lattice configurations for each cell surrounding $\mathbf{x}$ in each diagonal direction that is in contact with a boundary [15]. For this purpose we can locally define the integer $I(\mathbf{x}) = \sum_{j=1}^{8} Z(\mathbf{x}_j) 2^{8-j} \in \{0, 1, ..., 255\}$, where $\mathbf{x}_j$ surrounds $\mathbf{x}$. For the 256 configurations we are locally going to interpolate the corners of the digital media by constructing new surfaces build up by triangular shapes. The procedure we outline here for locally generating these improved linear boundaries is equivalent to Marching cubes [34]. However, in our case we have two choices. We can calculate all such surfaces in the domain, store them in a lookup table, and use their reduction factor in surface area together with the boundary condition of Eq. (9). Alternatively, we can let each walker that first interacts with a given boundary perform this procedure on the fly, which is clearly more efficient when the number of walkers are few.

2.3. *Outer boundaries*

The domains of the chalk samples may be large but are always finite. Hence we need to treat walkers that escape the cubic (N^3) domain via pore-voxels in one of the six outer surfaces. The method we use is

to introduce a walker in a random pore-voxel in the opposite outer surface of which it escaped. This procedure is common in the literature [11, 12] and our simulation results are in fact fairly insensitive to the way we treat those walkers escaping the domains. This is a consequence of the large cubic domains we use and therefore the probability of escaping the domain is much smaller than to interact with the pore surface.

2.4. *Statistical accuracy of the solution*

When discussing the convergence of a stochastic simulation as outlined above we generally need to fulfill the following conditions.

(1) The number of trajectories should be sufficient to obtain results of a certain statistical significance.

(2) The step size should be small enough in order to probe all of the small scale geometry of the media. Note that this is directly connected to the resolution used when producing the digital media.

If conditions (1) and (2) are fulfilled, one can accurately simulate diffusion processes with Dirichlet ($\rho \to \infty$) and Neumann ($\rho \to 0$) boundary conditions in Eq. (2). In the context of NMR relaxation this limits would mean that all particles were affected by surface relaxation ($\rho \to \infty$), or that all were reflected back uneffected ($\rho \to 0$).

However, for Robin boundary conditions ($0 < \rho < \infty$) we require the following additional probability based modeling of the surface relaxation.

(3a) A relation (algorithm dependent) between the local probability for surface relaxation, p_S, and the function $\rho(\mathbf{x}, t)$ describing the local surface relaxation parameter.

(3b) A local description of the surface area for a digital media.

We believe that neither (3a) or (3b) is always satisfactorily treated in the literature. Although (3a) has been discussed for some specific algorithms and geometries, e.g., [8, 13], it is widely misused in the literature for other types of algorithms. The results from NMR relaxation simulations are today therefore usually fitted to experimental data with help of a superfluous free parameter.

Condition (3b) about the geometry is generally difficult, since we do not know the true geometry of the media from which our digital images have been extracted. We will use a simple linear interpolation of the geometry, which is then merged into the boundary conditions for surface relaxation. The general concept was introduced in [15] and was there described in detail for two spatial dimensions under the name *linear local boundary conditions* (LLBC).

In the present article we have combined the results of Eq. (9) and the surface interpolation described in Sect. 2.2 to treat the points (3a) and (3b) by constructing linear local Robin boundary conditions to be used in Cartesian random walks in three-dimensions and benchmarked their usefulness for modeling NMR time series in digital media. Although interpolating digital media have been extensively discussed for many years it does not appear to have been spread to the NMR practitioners.

Regarding condition (1) above we have seen that the accuracy of the obtained solution at any given time is dependent on the number of walkers at $t = 0$. The computational time of our software is roughly linear in the number of trajectories, but the statistical standard error in the total magnetisation is expected to scale as the square-root of the number of trajectories.

All stochastically sampled data presented for three-dimensional samples in this article is averaged over 10^6 initial trajectories. For the corresponding level of statistical accuracy the standard errors are comparable to the linewidth of the curves presented in the figures of the full time intervals (not for zoom-in figures, see e.g. Fig. 3).

With the given hardware (an octa core workstation with 96 Gb RAM) and software (Python code with the demanding subroutines in C) at hand for this study, a simulation with 10^6 trajectories walking on $\sim 10^9$ voxels the total computational time per sample was in the order of 10 hours. Hence, for example $\sim 10^3$ trajectories only take in the order of 10 s to process, which is fast enough for in-field analysis of geophysical samples. Consequently, the level of statistical accuracy of the relaxation data generated from 10^3 trajectories may be investigated in an ongoing applied project.

Regarding point (2) we used a computational lattice that agrees with the resolution in the CT-images and with the cubic test domain we got convergence to the correct solution (from Eq. (18)) in the limit of $\Delta r \to 0$.

3. Benchmarking of the numerical method

We start this Sect. with a qualitative discussion of the quantitative results to be presented.

As shown in [15], the initial slope of the total magnetisation in three-dimensions, both for the pore-domain Ω beeing a ball of radius R_0 and a cube with sidelength $2R_0$, is given by

$$\frac{1}{\mathcal{M}(0)} \left.\frac{d\mathcal{M}(t)}{dt}\right|_{t=0} = -\frac{3\rho}{R_0}. \tag{12}$$

Results of the type in Eq. (12) for the specific geometries presented here are generally valid for any connected pore with a uniform initial condition [15] with the general result being

$$\frac{1}{\mathcal{M}(0)} \left.\frac{d\mathcal{M}(t)}{dt}\right|_{t=0} = -\rho\frac{S}{V}. \tag{13}$$

Here, S represents the pore surface and V the pore volume. Hence, for the ball we have $S = 4\pi R_0^2$ and $V = 4\pi R_0^3/3$, and for the cube $S = 6\,(2R_0)^2$ and $V = (2R_0)^3$. This explains Eq. (12) in those cases. Now we can note that for fast diffusion (in relation to the connectedness of the pore) the density is kept approximatelly uniform and the result (13) holds for any time, i.e.,

$$\mathcal{M}(t) \simeq \mathcal{M}(0)\,\mathrm{e}^{-\rho\frac{S}{V}t}. \tag{14}$$

Many estimates based on the pore distribution function of a porous media are based on the approximation (14) [33]. This is also in agreement with the interpretation of a lowest dominating mode

$$\mathcal{M}(t) \simeq \mathcal{M}(0)\,\mathrm{e}^{-\lambda_1 t},\ \lambda_1 \simeq \rho S/V, \tag{15}$$

as discussed in [19].

Generally a larger value of the surface relaxation parameter ρ will cause the magnetic moment $M(\mathbf{x},t)$ to decay more rapidly close to surfaces and more modes are needed to describe $M(\mathbf{x},t)$. Hence the approximations (14) and (15) gradually fails. There is also a qualitative dependence on the geometry of the pore-domain since there is more surface area close to corners. Hence sharp corners makes the magnetic moment more multiexponential.

With the true (lowest) eigenvalues, λ_j, for the ball and cube with physical parameters such as $\rho S/V = 3$ and $\rho = R_0 = D_0 = 1$ reported in Table 1, we can compare the approximation in (15)

$$\lambda_1^{ball} = 2.4674 \approx 3,\ \lambda_1^{cube} = 3{\cdot}0.74017 = 2.2205 \approx 3. \tag{16}$$

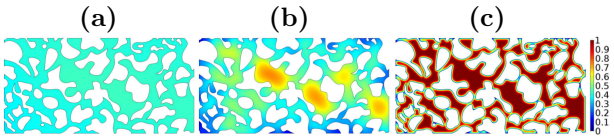

Fig. 1. Spatial patterns of the calculated relative NMR data, $M(\mathbf{x},t)/M(\mathbf{x},0)$, in different parameter regimes at the time $t = 1$ s obtained with an "extremely fine" grid on the FEM software Comsol v. 4.2. (a) Inter-pore *fast* diffusion: the diffusion constant is here $D_0 = 10^{-7}$ m^2/s; (b) Intra–pore diffusion: $D_0 = 10^{-9}$ m^2/s; (c) *Slow* diffusion regime: $D_0 = 10^{-11}$ m^2/s. We have kept the surface relaxation parameter fixed $\rho \simeq 10^{-5}$ m/s in all cases, such that the ratio T_{D_0}/T_ρ (see Eqs. (3) and (4)) is increasing by a factor 100 from (a) to (b), and from (b) to (c).

3.1. *Comparison with FEM calculations in two-dimensional artificial porous media*

For two-dimensional domains of limited size it is still doable to use an extremely fine gridded finite element simulations (FEM) which in effect interpolates the original digital domain. The complexity of these calculations were relatively low and could be carried out on a standard PC in the order of minutes. We therefore compare the random walk method with and without the LLBC correction presented, with FEM simulations for a two-dimensional artificial porous media that is depicted in Figure 1. Examples of spatial patterns for the magnetic moment $M(\mathbf{x},t)$ for a certain time are presented in Figure 1. Subfigure (a) shows an example of fast diffusion where diffusion between different pores happens *faster* than surface relaxation, so called inter-pore diffusion; subfigure (b) shows an intermediate example where the diffusion is efficient only within the smaller pores, while large (colour code yellow) pores still have a strong amplitude left; finally in (c), the diffusion is so slow that in effect only the (one-dimensional) surface have been affected by the relaxation at $t = 1$.

We can obtain the total magnetisation as a function of time, see Figure 2, via Eq. (5), equivalent to integrating spatial patterns as in Figure 1 for each time. It is clearly seen that the local boundary conditions are superior in approximation the FEM results, that are here considered as reference curves.

3.2. *Benchmarking of the method for a ball and a cube*

In three dimensions we have first tested our implemention of the LLBC by benchmarking against

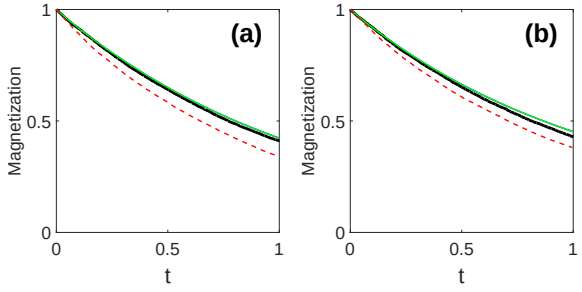

Fig. 2. Total magnetisation as a function of time. The upper (green) thin curves are from FEM calculations with an "extremely fine" grid in the FEM software Comsol v. 4.2. The lowest (red) dashed curves are calculated with the original Cartesian random walk method for two-dimensional domains, while the mid (black) thick curve is calculated using the improved (LLBC) random walk method. The two-dimensional media had $548 \times 274 \sim 10^5$ pixels with a resolution of $\Delta r = \Delta x = \Delta y = 1.17 \cdot 10^{-6}$ m, hence the physical size of the media was in the order of ~ 0.5 mm. A realistic parameter value for the diffusion constant in brine is $D_0 \simeq 2 \cdot 10^{-9}$ m^2/s [7], and we show here two 2D examples with: Fig. (a) $D_0 = 10^{-9}$ m^2/s; and Fig. (b) $D_0 = 10^{-8}$ m^2/s. The surface relaxation parameter was kept fixed $\rho \simeq 10^{-5}$ m/s [9] and no volume relaxation ($T_V \to \infty$) was present. The number of initial trajectories is 10^4 for this two-dimensional geometry, which is enough for the standard deviation to be in the order of the thickness of the linewidths in the plots.

analytic solutions for simple geometries, as was done for two dimensions in [15]. As the first analytic reference, we present a series expansion of the solution for the total magnetisation (with $T_V \to \infty$, see Eq. (6)) of a ball with uniform initial conditions, i.e., $M(\mathbf{x}, 0) = M_0$ [19] giving

$$\mathcal{M}(t) = 12\mathcal{M}(0) \times \sum_{j=1}^{\infty} \frac{\left[\sin\left(\sqrt{\lambda_j}\right) - \sqrt{\lambda_j}\cos\left(\sqrt{\lambda_j}\right)\right]^2}{\lambda_j^{3/2}\left[2\sqrt{\lambda_j} - \sin\left(2\sqrt{\lambda_j}\right)\right]} \mathrm{e}^{-\frac{D_0}{R_0^2}\lambda_j t}, \tag{17}$$

where the eigenvalues λ_j are solutions of the equation

$$1 - \sqrt{\lambda_j}\cot\left(\sqrt{\lambda_j}\right) = R_0\rho/D_0.$$

In Figure 3 we compare numerical solutions with and without LLBC to the analytic solution of Eq. (17). We see that LLBC improves the result for the ball, while a systematic deviation is still present.

To further illustrate the dramatic effect of the digitized surface of the ball (sphere) we have also plotted numerical results obtained from a radial random walk, which is the same data as the "$D = 3$"-curve in Figure 1 (a) of [15], that converge to the analytic solution given a small enough discretization Δr of the radius of the ball.

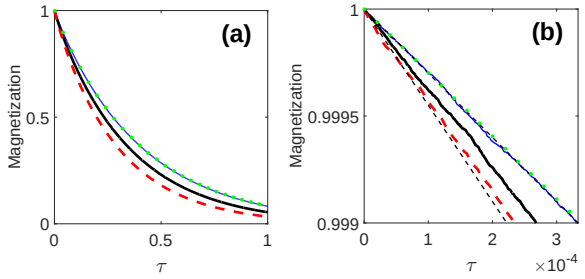

Fig. 3. Total magnetisation of the ball. In (a) the full time interval is shown in the dimensionless time variable $\tau = D_0 t/R_0^2$. The (red) thick dashed curves show the result from the Cartesian random walk with the original boundary condition. The (black) thick solid curves are from the random walk with the LLBC improvement incorporated. The analytic solution of Eq. (17), with 27 terms included in the sum such that $1 - \sum_j b_j \simeq 10^{-6}$, is shown with (green) dots. Solid (blue) curves show the result obtained with a radial random walk [15]. In (b) we show in addition two analytic short time asymptotes as (black) thin lines. The upper right line has the slope $-3\rho/R_0$ (according to Eq. (12)), while the lower left line has the slope $-9\rho/(2R_0) = -\rho \cdot 6 \cdot \pi R_0^2/\left(4\pi R_0^3/3\right)$.

The second of the two simple three-dimensional geometries we consider is the cube. While the results of the D-dimensional case were derived for dimensionless variables in [15] for different initial conditions with help of Sturm-Liouville theory, we here give explicitly the total magnetisation for the cube with uniform initial conditions

$$\mathcal{M}(t) = 8\mathcal{M}(0) \times \left[\sum_{j=1}^{\infty} \frac{\sin^2\left(\sqrt{\lambda_j}\right)}{\sqrt{\lambda_j}\sin\left(\sqrt{\lambda_j}\right)\cos\left(\sqrt{\lambda_j}\right) + \lambda_j} \mathrm{e}^{-\frac{D_0}{R_0^2}\lambda_j t}\right]^3. \tag{18}$$

Now the eigenvalues λ_j are solutions of the equation

$$\sqrt{\lambda_j}\tan\left(\sqrt{\lambda_j}\right) = R_0\rho/D_0.$$

In Figure 4 we compare numerical solutions with and without LLBC to the analytic solution of Eq. (18). For the (non-rotated) cube the LLBC have no effect since the result is already exact. When rotating the cube, with respect to the coordinate axis, large deviations occurs (dashed curves) that are only partly corrected with LLBC.

For the discussion to follow and the convenience of the readers in checking their own codes for NMR relaxation we include the necessary numbers in Table 1 in order to use the formulas of Eqs. (17) and (18) in practice. From Eq. (17) we define b_j as the coefficients in the series for the ball (b), while for Eq. (18) we define c_j =

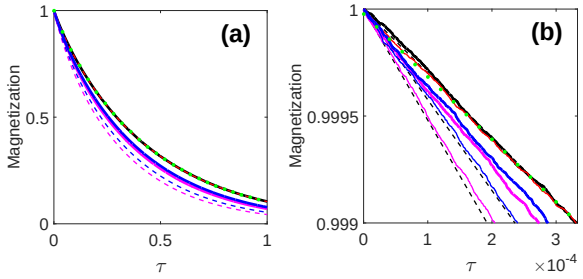

Fig. 4. Total magnetisation of the cube in different orientations. (a) shows the full time interval in the dimensionless time variable $\tau = D_0 t/R_0^2$. The (red) thick dashed curves shows the result from the Cartesian random walk with the original boundary condition. The (black) thick solid curves are from the random walk with the LLBC improvement incorporated. The blue pair of curves, dashed line for original boundary condition, thick solid line for the LLBC incorporated, shows the result for a cube rotated $(\pi/8,\ \pi/8)$. The magenta pair of curves shows the result for a cube rotated $(\pi/4,\ \pi/4)$. The analytic solution of Eq. (18), with 29 terms included in the sum such that $1-2\sum_j c_j \simeq 10^{-6}$, is shown with (green) dots. (b) shows in addition three analytic short time asymptotes as (black) thin dashed lines. The upper right dashed line (covered by other symbols) has the slope $-3\rho/R_0$ (according to Eq. (12)), while the mid dashed line has the slope $-3\sqrt{2}\rho/R_0$ and the lower left dashed line has the slope $-3\sqrt{3}\rho/R_0$.

$\sin^2\left(\sqrt{\lambda_j}\right) / \left[\sqrt{\lambda_j}\sin\left(\sqrt{\lambda_j}\right)\cos\left(\sqrt{\lambda_j}\right) + \lambda_j\right]$ as the terms in the corresponding series

$$\mathcal{M}(0)^{1/3} = \mathcal{M}(0)^{1/3}\, 2\sum_{j=1}^{\infty} c_j = 1$$

for the cube (c), see Table 1.

j	λ_j ball (17)	b_j ball	λ_j cube (18)	c_j cube
1	2.4674	0.98553	0.74017	0.49305
2	22.207	0.012167	11.735	$6.2044 \cdot 10^{-3}$
3	61.685	$1.5769 \cdot 10^{-3}$	41.439	$5.5554 \cdot 10^{-4}$
4	120.90	$4.1047 \cdot 10^{-4}$	90.808	$1.1866 \cdot 10^{-4}$
5	199.86	$1.5021 \cdot 10^{-4}$	159.90	$3.8627 \cdot 10^{-5}$
6	298.56	$6.7313 \cdot 10^{-5}$	248.73	$1.6034 \cdot 10^{-5}$
7	416.99	$3.4506 \cdot 10^{-5}$	357.30	$7.7895 \cdot 10^{-6}$
8	555.17	$1.9467 \cdot 10^{-5}$	485.61	$4.2232 \cdot 10^{-6}$
9	713.08	$1.1800 \cdot 10^{-5}$	633.65	$2.4827 \cdot 10^{-6}$
10	890.73	$7.5624 \cdot 10^{-6}$	801.44	$1.5530 \cdot 10^{-6}$

Table 1
For the 3D test cases presented in Figures 3 and 4 we here give the first 10 *eigenvalues and corresponding coefficients for the parameter values* $\rho = R_0 = D_0 = 1$ *(i.e. intermediate diffusion regime). Note the qualitative difference in the values for the ball and cube for a given* j*. This is due to the difference in the definition of the series, see Eqs. (17) and (18) respectively.*

Property	Aalborg	Aal., LLBC	Limestone	Lim., LLBC
N	696	696	1279	1279
Δr [nm]	21.47	21.47	25	25
V $[(\Delta r)^3]$	156789057	156789057	1043737196	1043737196
S $[(\Delta r)^2]$	27291763	20738034	61403293	48152708
$\phi = \frac{V}{N^3}$	0.465	0.465	0.499	0.499
$SSA = \frac{S}{N^3}$ $[(\Delta r)^{-1}]$	0.0809	0.0615	0.0293	0.0230
SSA [m^2/g]	1.4	1.1	0.43	0.34

Table 2
Data for the two real samples described in Sect. 4.1. Here V *is the pore volume,* S *the pore surface, and* ϕ *the porosity of the digital domains. The specific surface area (SSA) in the last row has been estimated using a density of* 2.7 *g/cm*^{3} *for calcite, which is the dominant compound of both samples [38].*

4. NMR relaxation in large complex domains

After having benchmarked LLBC with an artificial 2D porous media in Sect. 3.1, and with the analytic solutions of the ball and the cube in 3D in Sect. 3.2, we now apply LLBC to large complex digital domains from CT-images of chalk.

4.1. *Complex geometries, digital images of chalk*

A limestone sample was taken from an outcrop at Rdvig (Stevns Klint) in Denmark. A subsample ($\sim$ 500 μm in diameter) of this sample was imaged using the holotomography setup at the former ID22 [35] at the European Synchrotron Radiation Facility in Grenoble, France at four resolutions: 320, 100, 50 and 25 nm voxel size [36]. For the purpose of this work, we have chosen the data set at 25 nm voxel size to ensure the best possible result. As an example of a very complex pore geometry, we collected samples of chalk from a quarry in Aalborg, Denmark. Using a focused gallium ion beam in a scanning electron microscope, we produced cylindrical samples of $\sim$ 20 μm in diameter fit for imaging using the recently developed ptychography method. Imaging itself was performed at the Swiss Light Source in Villigen, Switzerland at the cSAXS beamline [37] resulting in a voxel size of 21.47 nm. Basic properties for the two digital domains from the two chalk samples, in part illustrated in Figure 5, are presented in Table 2.

The corresponding NMR relaxation for Aalborg chalk and limestone are seen in Figure 6.

Our first sample, Aalborg chalk, was represented by a volume of 696^3 voxels. The second sample, lime-

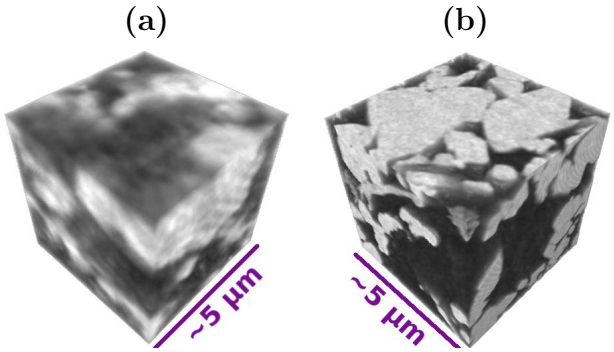

Fig. 5. Examples of zooming in on regions in the CT-images for the two 3D chalk samples. To the left limestone (a) and to the right Aalborg chalk (b). Black ($Z = 1$) voxels constitutes the pore domain (assumed to be filled with brine). White ($Z = 0$) voxels represents regions of homogenous chalk. Aalborg chalk (b) contains a more complex pore morphology and was imaged with ptychographic X-ray nanotomography, which explains the sharper image compared to (a). Since the side length of the full samples are in the order of $N\Delta r \simeq 25$ μm (Table 2), the subvolumes shown here represents only about 1% of the chalk sample domains in our calculations.

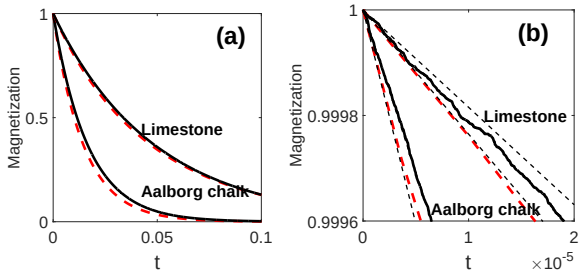

Fig. 6. Total magnetisation of the chalk samples, described in Sect. 4.1, for the relevant full time interval in seconds in (a). A zoom in for a comparison with the analytic short time asymptotes in (b). The (red) thick dashed curves show the result from the Cartesian random walk with the original boundary condition. The (black) thick solid curves are from the random walk with the LLBC improvement incorporated. In (b) four analytic short time asymptotes are shown as (black) thin dashed lines. The asymptotes all have the slope $-\rho S/V$ (according to Eq. (13)), while the ratio of the pore surface S and the pore volume V varies with the sample and the boundary condition in use, see Table 2.

stone, had 1279^3 voxels. In order to test the ability to later analyse even larger experimental samples, we have treated artificial porous media with more than $\sim 10^{10}$ voxels (i.e. ~ 10 times the numbers of the real data in this study) on a single PC. Due to the independence of individual trajectories, it is in effect the RAM memory that limits the size of the sample one can efficiently handle with a given hardware.

4.2. *Results of the total magnetisation in chalk*

The results of applying the numerical methods of Sect. 2 to the chalk samples are presented in Figure 6. We can observe qualitatively different results for the NMR relaxation curves of the Aalborg chalk and the limestone samples. In fact their half times, $T_{1/2}$, differ by more than a factor of two (see Fig. 6 (a)). The half times are in the order of $T_{1/2} \sim 10$ ms for the Aalborg chalk and of $T_{1/2} \sim 30$ ms for the limestone. According to Table 2 the two samples have similar porosity but quite different specific surface area. We interpret the faster relaxation for the Aalborg chalk as mainly a consequence of its richer surface structure and narrower pore throats. From Figure 5, we can estimate that most pores are of size much smaller than of 10 μm. Hence, the discussion under Eqs. (3) and (4) suggest that we are in the regime of fast diffusion for both samples. Then we can expect the approximation of Eq. (14) to be relevant. Indeed we can qualitatively obtain the half times as $T_{1/2} \sim \ln 2 \cdot V/(\rho S) \simeq 8.5 - 11$ ms for the Aalborg chalk and of $T_{1/2} \simeq 29 - 38$ ms for the limestone (the ranges are presented due to the two different columns for each sample in Table 2). However, by plotting the curves corresponding to Eq. (14) in the same graph as the numerically obtained relaxation curves (Fig. 6) important quantitative differences shows up, so a more accurate description is necessary for a quantitative analysis.

As mentioned earlier (e.g.) for brine we have in addition that the volume relaxation time is $T_V \simeq 3.1$ s and the true (experimental) relaxation curves for the chalk samples are as those in Figure 6 but multiplied with the common factor e^{-t/T_V} (see Eq. (6)). This lower the half times according to $T_{1/2} \sim \ln 2/(\rho S/V + 1/T_V)$, which is only about 1% shorter than the half times stated above.

4.3. *Decomposition of the total magnetisation into Laplace components*

By a mathematical inversion process on the NMR relaxation data, it is possible to obtain the familiar T-distribution curve, which reflects the distribution of the pore surface-to-volume ratio of the media [9].

The starting point for presenting our method for a signal analysis of the total magnetisation is the Laplace transform of the real decomposition $F(\beta)$

$$\mathcal{M}(t) = \int_0^\infty F(\beta)\, \mathrm{e}^{-\beta t} d\beta. \tag{19}$$

Finding F given $\mathcal{M}$ is an ill-posed inverse problem [39]. Most commonly used methods retrieve a continuous approximation for the distribution $F(\beta)$, a so called T-distribution curve, using some sort of regularization to pick an F with small support. Alternatively, one may use the complex frequency estimation technique ESPRIT [40] in order to find few coefficients $d_j > 0$ and corresponding inverse times $\beta_j = 1/T_j > 0$, such that the distribution

$$F(\beta) = \sum_j d_j \delta(\beta - \beta_j), \tag{20}$$

via the Laplace transform (19), gives an approximation of the total magnetisation. In other words we here seek representations of the form

$$\mathcal{M}(t) \simeq \sum_{j=1}^{m} d_j \mathrm{e}^{-t/T_j}. \tag{21}$$

Given that $\mathcal{M}$ is of the form (21), ESPRIT is guaranteed to find the precise parameters. However, in the presence of noise, this may not be the case, and it can then be beneficial to use more advanced techniques to pretreat the data in order to avoid, e.g., complex frequency components. The algorithm presented in [41] is tailormade for this purpose, which aims to minimize the L^2-error

$$\mathcal{N} = \sqrt{\int_0^{t_2} \left| \mathcal{M}(t) - \sum_{j=1}^{m} d_j \mathrm{e}^{-t/T_j} \right|^2 dt}, \tag{22}$$

while at the same time enforcing the parameters T_j to be real. We here refer to this method as "real exponents ESPRIT".

We also present the results from a traditional method, using Tikhonov Regularized Inversion (TRI) [42]. The regularization parameter in TRI was chosen according to the discrepancy principle [43] with an estimated error level of 10^{-3}, obtained from a comparison between a numerical and an analytic solution of the cube.

In Figure 7 we compare the analytic solution for the ball to the ESPRIT algorithm and the TRI method. Since the analytic solution is used, ESPRIT is guaranteed to find all exponents and coefficients within machine precision. In Figure 8 we apply the real exponents ESPRIT method and the TRI method to numerical data. The numerical data is obtained using the methods introduced in Sect. 2 to the ball (a) and the cube (b). The random

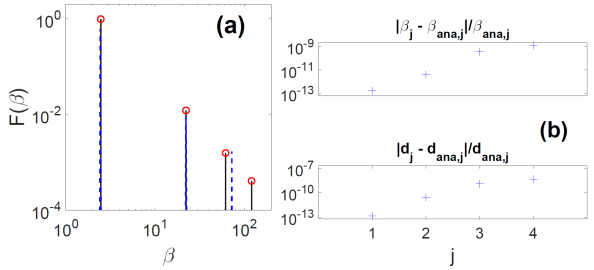

Fig. 7. Decomposition of the analytic total magnetisation of the ball, using four terms in Eq. (17). (a) Loglog plot of numerically obtained coefficients and exponents, vertical (black) lines shows the discrete result from ESPRIT, while the continuous (blue) dashed-curve are from the Tikhonov regularized inversion. The original four analytic datapoints, see Table 1, are shown as (red) open circles. (b) Relative deviation for the four numerically obtained data points in (a) using ESPRIT.

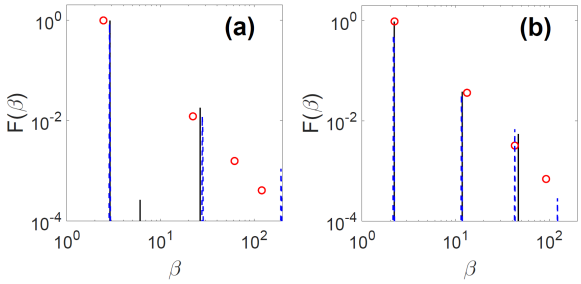

Fig. 8. Decomposition of the numerical total magnetisation of the ball (a) and cube (b). Loglog plots of numerically obtained coefficients and exponents, vertical (black) lines shows the discrete result from real exponents ESPRIT, while the continuous (blue) dashed-curves are from the Tikhonov regularized inversion. The four (red) circles in each plot shows the four dominating analytic datapoints for the corresponding geometries (from Table 1). Since the LLBC is not exact for the ball, a small systematic mismatch in (a) is expected for all terms.

walk method with LLBC introduce small structural errors in the signal. This can be seen as noise and a systematic deviation of the mean, respectively. Therefore, it is not clear that analytic positions of the exponents give the best fit to the numerical signal, i.e., that corresponding values of T_j and d_j minimize (22). Further testing would be needed in order to draw conclusions about the reliability of the two methods presented. The presented values also depend on choosing certain parameters for both methods, however, Figure 8 indicate that both methods do a good job in retrieving the two main exponential terms in the signal.

To further validate the result from the real exponents ESPRIT method we calculate $\mathcal{N}$, for the corresponding few term approximations (21), according

Norm	$\mathcal{N}_{ball,\,ana.}$	$\mathcal{N}_{ball}$	$\mathcal{N}_{cube}$	$\mathcal{N}_{L}$	$\mathcal{N}_{Aa}$
$m=1$	$1.3\cdot10^{-3}$	$2.0\cdot10^{-3}$	$4.8\cdot10^{-3}$	$2.9\cdot10^{-4}$	$3.2\cdot10^{-5}$
$m=2$	$3.6\cdot10^{-5}$	$1.4\cdot10^{-4}$	$3.5\cdot10^{-4}$	$4.8\cdot10^{-5}$	$3.1\cdot10^{-5}$
$m=3$	$9.0\cdot10^{-7}$	$9.3\cdot10^{-5}$	$1.6\cdot10^{-4}$	$4.8\cdot10^{-5}$	-
$m=4$	$2.2\cdot10^{-14}$	$9.0\cdot10^{-5}$	$1.5\cdot10^{-4}$	-	-
t_2	0.927	0.789	1.02	0.113 [s]	0.0382 [s]

Table 3

Norm of the deviation between numerical data and the real exponents ESPRIT approximation with m-terms, see Eq. (22). The first result column, $\mathcal{N}_{ball,\,ana.}$, reports the norms when comparing an analytic series for the ball with four terms (see Eq. (17) and Table 1) with the few terms expansion (21) according to ESPRIT. If we instead would have m-terms in the analytic series for the ball, the ESPRIT method for m-terms is exact for noiseless data up to numerical errors [40], see row with $m = 4$ and the two subplots in Figure 7 (b). The four remaining columns, $\mathcal{N}_{ball}$, $\mathcal{N}_{cube}$, $\mathcal{N}_{L}$, and $\mathcal{N}_{Aa}$, reports the norms when comparing the real exponents ESPRIT obtained approximation with m-terms to numerical data for the ball, cube, limestone (L), and Aalborg chalk (Aa), using LLBC in all four cases. For the chalk samples, which are in the fast diffusing regime, the norm do not change substantially by adding more than 2-3 terms (the two most right columns). The lengths of all the vectors tested here are odd numbers in the order of 10^3. The truncation in the numerical data is set to the smallest time, t_2, for which the total magnetisation fulfills $\mathcal{M}(t)/\mathcal{M}(0) < 0.1$, and is reported in the lowest row.

to the discrete version of (22) for different number of terms, m, and with a relatively large upper integration limit, t_2, specified in Table 3. Since the result of the real exponents ESPRIT algorithm is dependent on a parameter τ and the number of iterations, we stress that the reported norms are not unique. The lowest exponents obtained with real exponents ESPRIT for the chalk samples, $\beta_1 \simeq 20.4\ \mathrm{s}^{-1}$ for Limestone and $\beta_1 \simeq 60.3\ \mathrm{s}^{-1}$ for Aalborg chalk, is in agreement with the estimates of the half-times $T_{1/2} = \ln 2/\beta_1$ given in Sect. 4.2.

5. Discussion and summary

For the NMR relaxation simulation described here, we started from a deterministic partial differential equation and then used an equivalent stochastic particle formulation for the calculation. As expected from the previous investigation [15], the systematic errors for the NMR relaxation caused by the digitalisation of the 2D surfaces within the 3D geometrical objects occurs qualitatively different depending on the object and its orientation in relation to the coordinate system in a digital image. Here we have quantified those systematic errors and showed how they can be reduced for the ball and the cube in 3D and for an artificial 2D porous media for which comparative finite element calculations were tractable.

For two complex digital domains representing different chalk samples, that had similar porosity, but with substantially different specific area, we found qualitatively different relaxation dynamics. Additionally for each of those complex domains the relaxation curve without local boundary conditions were markably lower and we expect to have removed a major part of the errors between the true NMR relaxation and its simulated dynamics.

For the inversion analyse of the NMR relaxation data, commonly called T-distribution curve, we have introduced and benchmarked a new method to the field.

Acknowledgement

The authors from the University of Copenhagen would like to thank Innovation Fund Denmark and Maersk Oil for funding this research through the project P^3 — *Predicting Petrophysical Parameters.* We acknowledge Danscatt for supporting datasampling and thank Ye Zhang for providing software for the Tikhonov regularization.

References

[1] D. Müter, H. O. Sørensen, H. Bock and S. L. S. Stipp, The Journal of Physical Chemistry C **119**, 10329 (2015)
[2] I. T. Lin, H. C. Yang and J. H. Chen, Appl. Phys. Lett. **102**, 063701 (2013)
[3] E. O. Fridjonsson, J. D. Seymour, L. N. Schultz, R. Gerlach, A. B. Cunningham and S. L. Codd, Journal of Contaminant Hydrology **120-121** (2011) 79-88
[4] M. M. Tomadakis and T. J. Robertson, J. of Chem. Phys. **119**, 1741 (2003)
[5] S. D. Senturia and J. D. Robinson, SPE J **10**, 237 (1970)
[6] M. H. Cohen and K. S. Mendelson, Journal of Applied Physics **53**, 1127 (1982)
[7] W. E. Kenyon, Nuclear Geophysics **6**, 153 (1992)
[8] J. Finjord, A. Hiorth, U. H. Lad, S. M. Skjæveland, Transp Porous Med Trans. Porous Med. **69** (2007), 33
[9] B. Vincent, M. Fleury, Y. Santerre, B. Brigaud, J. of Appl. Geophysics **74** (2011), 38-58
[10] O. Mohnke, Water Resour. Res. **50**, 5309 (2014)
[11] P. E. Øren, F. Antonsen, H. G. Rueslåtten and S. Bakke, in *Proceedings of the SPE Annual Technical Conference and Exhibition, San Antonio, 2002*, SPE 77398
[12] O. Talabi, S. AlSayari, S. Iglauer and M. J. Blunt, Journal of Petroleum Science and Engineering **67**, 168 (2009)
[13] D. J. Bergman, K. J. Dunn, L. M. Schwartz and P. P. Mitra, Phys. Rev. E **51**, 3393 (1995)
[14] G. Jin, C. Torres-Verdn, E. Toumelin, Journal of Magnetic Resonance **200**, 313 (2009)

[15] M. Ögren, Eur. Phys. J. B (2014) **87**: 255
[16] I. I. Rabi, J. R. Zacharias, S. Millman and P. Kusch, Phys. Rev. **53**, 318 (1938)
[17] F. Bloch, Phys. Rev. **70**, 460 (1946)
[18] H. Torrey, Phys. Rev. **104**, 563 (1956)
[19] K. R. Brownstein and C. E. Tarr, Phys. Rev. A **19**, 2446 (1979)
[20] O. Mohnke and N. Klitzsch, Vadose Zone J. **9**, 846 (2010)
[21] Y. Q. Song, Phys. Rev. Lett. **85**, 3878 (2000)
[22] D. S. Grebenkov, Review of Modern Physics **79**, 1077 (2007)
[23] M. J. Lizak, M. S. Conradi and C. G. Fry, Journal of Magnetic Resonance **95**, 548 (1991)
[24] Y. Q. Song, H. C. Gaede, T. Pietrass, G. A. Barrall, G. C. Chingas, M. R. Ayers and A. Pines, Journal of Magnetic Resonance **115**, 127 (1995)
[25] I. Karatzas and S. E. Shreve, *Brownian motion and stochastic calculus*, Springer Graduate Texts in Mathematics, 2.nd edition, 1991
[26] H. Risken, *The Fokker-Planck equation*, Springer 2.nd edition 1996
[27] N. G. van Kampen, *Stochastic processes in physics and chemistry*, Elsevier 3.rd edition 2008
[28] C. W. Gardiner, *Stochastic Methods*, Springer-Verlag, Berlin Heidelberg, 4.rd edition, 2009
[29] P. D. Drummond, P. Deuar, J. F. Corney, K. V. Kheruntsyan, Proceedings of the 16th International Conference on Laser Spectroscopy (ICOLS) (2003)
[30] M. Ögren, K. V. Kheruntsyan and J. F. Corney, Comput. Phys. Commun. **182** (2011) 1999
[31] S. Torquato and In Chan Kim, Appl. Phys. Lett. **55**, 1847 (1989)
[32] J. R. Banavar and L. M. Schwartz, Phys. Rev. Lett. **58**, 1411 (1987)
[33] K. S. Mendelson, Phys. Rev. B **41**, 562 (1990)
[34] T. S. Newman and H. Yi, Computers and Graphics **30** 854 (2006)
[35] A. Koch, C. Raven, P. Spanne and A. Snigirev, J. Opt. Soc. Am. A **15**, 1940 (1998)
[36] D. Müter, H. O. Sørensen, D. Jha, R. Harti, K. N. Dalby, H. Suhonen, R. Feidenhans'l, F. Engstrøm and S. L. S. Stipp, Appl. Phys. Lett. **105**, 043108 (2014)
[37] M. Holler, A. Diaz, M. Guizar-Sicairos, P. Karvinen, E. Färm, E. Härkönen, M. Ritala, A. Menzel, J. Raabe and O. Bunk, Sci. Rep. **4**, 3857 (2014)
[38] H. O. Sørensen, S. S. Hakim, S. Pedersen, B. C. Christiansen, Z. I. Balogh, C. P. Hem, I. S. Pasarin, S. Schmidt, U. L. Olsen, J. Oddershede, C. Frandsen, R. FeidenhansL and S. L. S. Stipp Can. Mineral. **50**, 501 (2012)
[39] P. Berman, O. Levi, Y. Parmet, M. Saunders and Z. Wiesman, Concepts in Magnetic Resonance Part A **42**, 72 (2013)
[40] R. Roy and T. Kailath, Acoustics, Speech and Signal Processing, IEEE Transactions on **37**, 984 (1989)
[41] F. Andersson, M. Carlsson and H. Wendt, 24th European Signal Processing Conference (EUSIPCO), 326-330, (2016)
[42] R. L. Parker and Y. Q. Song, Journal of Magnetic Resonance **174**, 314 (2005)
[43] Per Christian Hansen, *Rank-Deficient and Discrete Ill-Posed Problems: Numerical Aspects of Linear Inversion*, SIAM 1998